## PAPER

Check for updates

# Study of Se/Te-doped Cu$_2$O as a hole transport material in perovskite solar cells

Liang Luo, [a] Bao Zhou,*[a] Zhenzhen Liu,[a] Qirong Zhao,[a] Chao Wang,[a] Zhuoqi Duan,[a] Zaixin Xie,[a] Xiaobo Yang[b] and Yongmao Hu [ab]

Theoretically, cuprous oxide (Cu$_2$O) is a particularly excellent potential material, for the hole transport layer (HTL) of perovskite solar cells (PSCs). However, the photoelectric conversion efficiency (PCE) of its experimental samples is still not ideal. The main reasons for this include the material, and inherent and interface defects of Cu$_2$O, but this can be improved by doping. In this research, Te- and Se/Te-doped Cu$_2$O were experimentally and numerically studied to check the improvement of the material and interface properties. It was found that, for both the electrical and optical properties, the Se/Te-doped Cu$_2$O performed considerably better than that which had been Te-doped and the pure Cu$_2$O. Compared with the pure Cu$_2$O thin film, the carrier mobility of the Se/Te-doped Cu$_2$O thin film is improved from 60 cm$^2$ V$^{-1}$ s$^{-1}$ to 1297 cm$^2$ V$^{-1}$ s$^{-1}$, and the bandgap changed from 2.05 eV to 1.88 eV. According to the results calculated using solar cell simulation software SCAPS, the cell efficiency of the Se/Te-doped Cu$_2$O is improved by 22% when compared to that of pure Cu$_2$O. This efficiency can be further improved to 34% by optimizing the thickness of the Se/Te-doped Cu$_2$O thin film and the defect density of states between the material interfaces.

## 1 Introduction

Cuprous oxide (Cu$_2$O) has good practical applications in fungicides, photocatalysis and solar cells because of its bandgap (2.0–2.2 eV), high light absorption coefficient, stable chemical properties, and so on.[1–3] For perovskite solar cells (PSCs), Cu$_2$O is an excellent inorganic material as the hole transport layer (HTL) because of its stability, inexpensiveness and ease of preparation when compared with organic materials, such as spiro-OMeTAD. Theoretically the photoelectric conversion efficiency (PCE) of Cu$_2$O-based PSCs can be as high as 28%,[4] but is found to be only about 18%,[5–7] experimentally, because of the material and interface defects, and difficulties with the preparation process. Tseng et al.[8] prepared Ag/GZO/SiO$_2$/MAPbI$_3$/Cu$_2$O/FTO reverse-structured PSCs by controlling the annealing temperature and deposition thickness of hole transport layer (HTL) and electron transport level (ETL), and the highest PCE found reached 18.4%. Liu et al.[9] prepared FTO/TiO$_2$/Cs$_{0.05}$FA$_{0.81}$MA$_{0.14}$PbI$_{2.55}$Br$_{0.45}$/Cu$_2$O/Au forward-structured PSCs with a surface modification of Cu$_2$O quantum dot films, and the PCE was improved to 18.9%, and the efficiency was still more than 90% of the initial one after 30 d of preservation. The interface performance between the perovskite

active layer (PAL, mainly MAPbI$_3$, FAPbI$_3$ and their derivatives) and HTL is very important. In addition to changing the preparation method and adding interface modification materials, it is also possible to improve the PCE of the solar cell by doping.

Some studies have shown that Se and Te doping can effectively reduce the crystal bandgap of the metal oxide materials, increase their light absorption range, improve their light absorption coefficient, and improve their carrier mobility and other properties. For example, Lin et al.[10] prepared nanotubes with different ratios of Te and Se/Te doped TiO$_2$, and found that the absorption coefficient was considerably enhanced in the visible spectrum, and the absorption edge had a strong red shift. Güney and Duman[11] prepared ZnSeO and ZnTeO thin films by changing the doping ratios of Se and Te, and obtained a significant decrease from 3.37 eV (pure ZnO) to 2.26–2.60 eV. Liu et al.[12] studied S-, Se- and Te-doped NaTaO$_3$ using the first-principles calculations, and obtained similar results for bandgap, in addition, the carrier mobility, and its difference between electrons and holes, was all significantly larger than that of pure NaTaO$_3$, which could effectively reduce the recombination of electrons and holes. Based on the previous work, it is also known that Te-doped Cu$_2$O can effectively reduce its bandgap and improve its conductivity.[13] However, the disadvantage of using Te is its biological toxicity. He and Su[14] found that alloying Te with Se (Te : Se = 1 : 0.43) could entirely eliminate the Te biological toxicity. This research focused on the photovoltaic properties of Se/Te-doped Cu$_2$O and complete simulations of its use as PSCs. Firstly, the electrical and optical properties of Te- and Se/Te-doped Cu$_2$O

*aCollege of Engineering, Dali University, Dali, Yunnan 671003, China. E-mail: zhoubao@dali.edu.cn*

*bFaculty of Materials Science and Engineering, Kunming University of Science and Technology, Kunming 650093, China*

were calculated theoretically. Then, the corresponding films were prepared experimentally to validate the theoretical results. Finally, the PSCs based on different HTLs (made of Te- and Se/Te-doped $Cu_2O$ thin films) were modelled and simulated using SCAPS software to check their performances.

# 2 Theoretical research

## 2.1 Models and calculation

The structural models can be seen in Fig. 1(a). Firstly, a $2 \times 2 \times 1$ $Cu_2O$ supercell, consisting of a total of 16 Cu atoms and 8 O atoms was constructed. Secondly, the positions of the three O atoms in the supercell were replaced with Te atoms to give Te : $Cu_2O$, with a Te content of 12.5%, as shown in Fig. 1(b). Lastly, by replacing one of the Te atoms in the center of supercell, with a Se atom to give Se/Te : $Cu_2O$, the proportion of the Se atoms was 4.17%, and the proportion of the rest of the Te atoms was 8.33%, as shown in Fig. 1(c). The electrical and optical properties of $Cu_2O$ before and after doping were obtained using first-principles calculations, and the changes in the material properties were compared.

## 2.2 Calculation results and discussion

**2.2.1 Structural properties.** After geometrical optimization, the structural properties of the three systems were obtained and are shown in Table 1. Compared to the pure $Cu_2O$, the doped $Cu_2O$ both underwent large lattice distortions, as follows. The change of cell angle $\alpha$ was the most obvious, whereas $\beta$ and $\gamma$ remained stable at about 90°. The lattice constant $a$ tended to increase by about 1.19 Å, which was basically equal to the radius of the Te atom minus the radius of the O atom, whereas $b$ and $c$ only changed a little. The volume has also increased, which was mainly due to Se and Te atoms form longer bonds with Cu atoms.[15] The total energy increased, and the stability of the system decreased.

**2.2.2 Electronic properties.** In terms of electronic properties, the CASTEP module was used to calculate the band structure, density of states (DOS), effective mass and Mulliken populations of the three systems.

Fig. 2 shows the band structures and DOS of the three systems. The calculated bandgap value of the pure $Cu_2O$ was 0.577 eV, the scissors operator was used and a correction value of 1.423 eV was given, and the experimental value of pure $Cu_2O$ was 2.0 eV,[16,17] as shown in Fig. 2(a). The valence band maximum (VBM) and the conduction band minimum (CBM) were both located at the high symmetry point G, that is, the direct bandgap, and the DOS showed a similar distribution to the band structure. From Fig. 2(b), it can be seen that the bandgap of Te : $Cu_2O$ decreased to 1.489 eV from the 2.0 eV of pure $Cu_2O$, which had reached the infrared region, and the Te 5p states were densely distributed at the Fermi level, which caused the O 2p states in the conduction band to move to the low energy end, and improve the localization of the electrons. From Fig. 2(c), it can be seen that the bandgap value of the Se/Te-doped $Cu_2O$ was increased to 1.545 eV when compared to that of the Te-doped $Cu_2O$. It was also known from previous work that the Se-doped $Cu_2O$ can increase its bandgap.[13]

The electron effective mass and hole effective mass for the three systems are shown in Table 2. As is known in $\mu = q\tau/m^*$, a smaller effective mass ($m^*$) implied a higher carrier mobility ($\mu$). From the calculated values of the effective masses, the effective mass of pure $Cu_2O$ was basically consistent with that found in the literature.[18,19] Compared with pure $Cu_2O$, the electron effective mass and hole effective mass in the doped systems were significantly reduced, and the carrier mobility was higher. Among the three systems, the carrier mobility of Se/Te : $Cu_2O$ increased more significantly.

The Mulliken populations of the central atoms and their adjacent atoms for the three systems are shown in Table 3. From the charge population in pure $Cu_2O$, it was seen that each
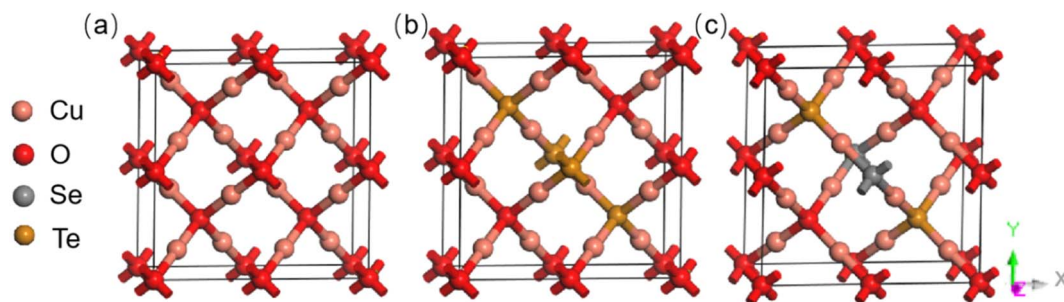


**Fig. 1** Structural model of (a) pure $Cu_2O$, (b) Te : $Cu_2O$, and (c) Se/Te : $Cu_2O$.

**Table 1** Cell angle, lattice parameter, volume, and total energy of the three systems

|  | $\alpha$ (°) | $\beta$ (°) | $\gamma$ (°) | $a$ (Å) | $b$ (Å) | $c$ (Å) | Volume (Å$^3$) | Total energy (eV) |
| --- | --- | --- | --- | --- | --- | --- | --- | --- |
| $Cu_2O$ | 90 | 90 | 90 | 4.22 | 8.46 | 8.46 | 301.39 | −27036.35 |
| Te : $Cu_2O$ | 78.27 | 89.97 | 89.94 | 5.41 | 8.54 | 8.53 | 385.82 | −26396.01 |
| Se/Te : $Cu_2O$ | 102.51 | 89.99 | 90.01 | 5.40 | 8.45 | 8.45 | 376.46 | −26433.76 |
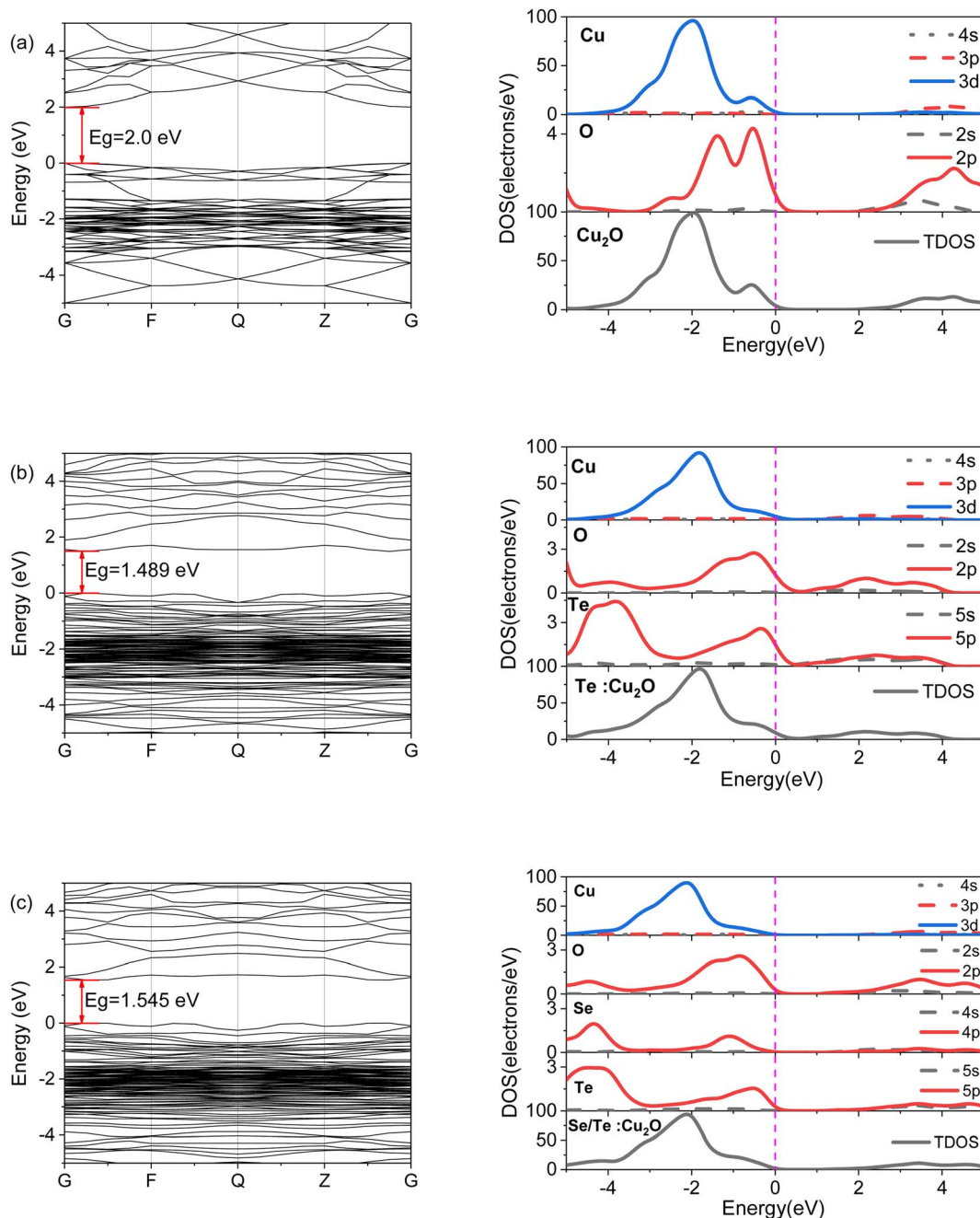
**Fig. 2** The band structure and DOS of (a) pure $Cu_2O$, (b) Te : $Cu_2O$, and (c) Se/Te : $Cu_2O$.

Cu loses $0.32e$, and O gains $0.63e$. For the Te-doped $Cu_2O$, the Te loses $1.36e$, the adjacent Cu gains $0.14e$, and the next-adjacent O gains $0.66e$. This shows that after Te doping, there was at least one free electron that caused the doped system to be metallized. For the Se/Te-doped $Cu_2O$, the Te shows a stronger ability to lose electrons, losing $1.57e$, the central Se loses $0.81e$, the adjacent Cu gains $0.1e$, and the next adjacent O gains $0.64e$. The Te has the most pronounced ability to lose electrons and becomes the center of the accumulation of the positive charges, which improved electron transport capacity and enhanced the electrical conductivity better than pure $Cu_2O$ did. According to the bond population, the Cu–O population of pure $Cu_2O$ was

**Table 2** Effective mass components (in units of $m_0$)

|      | $Cu_2O$ | Te : $Cu_2O$ | Se/Te : $Cu_2O$ | $Cu_2O$ [18] | $Cu_2O$ [19] |
|------|---------|--------------|-----------------|--------------|--------------|
| CBM  | $0.7358l$ | 0.4174     | 0.3754          | 0.6535       | 0.676        |
| VBM  | 2.7762  | 0.651        | 0.5643          | 2.4015       | 3.80         |

0.38, which indicated a strong interaction between the Cu and O atoms, and the presence of covalent bonds. With the doping of Te and Se/Te, the Cu–O bond population decreased, the covalence became weaker, and the bond length increased from 1.83

**Table 3** Charge population and bond population of pure $Cu_2O$, $Te : Cu_2O$, and $Se/Te : Cu_2O$

| | Charge population ($e$) | | | | Bond population/bond length (Å) | | |
|---|---|---|---|---|---|---|---|
| | Cu | O | Se | Te | Cu–O | Cu–Se | Cu–Te |
| $Cu_2O$ | 0.32 | −0.63 | — | — | 0.38/1.83 | — | — |
| $Te : Cu_2O$ | −0.14 | −0.66 | — | 1.36 | 0.37/1.87 | — | −0.19/2.43 |
| $Se/Te : Cu_2O$ | −0.10 | −0.64 | 0.81 | 1.57 | 0.32/1.87 | 0.06/2.24 | −0.43/2.44 |

Å to 1.87 Å. The bond lengths of Cu–Te and Cu–Se were about 2.44 Å and 2.24 Å, respectively, which were much larger than the Cu–O bond length, which was the main reason for the lattice distortion of the doped systems.

**2.2.3 Optical properties.** Fig. 3 shows the characterization of the optical properties for the three systems, with a correction value of 1.423 eV. Fig. 3(a) shows the real part of the dielectric functions of the three systems, with the zero point being the electrostatic dielectric function, and its values were 5.53, 10.22 and 9.32. The electrostatic dielectric function values of the doped systems were considerably larger than that of pure $Cu_2O$, which indicated the stronger polarization ability of the doped systems, and how much faster the light-excited carriers migrated in the crystal. Fig. 3(b) shows the absorption coefficients of the three systems, which were significantly improved in the visible region (1.55–3.26 eV). At 3.26 eV, the absorption coefficients of the three systems were $0.27 \times 10^5$ $cm^{-1}$, $0.93 \times 10^5$ $cm^{-1}$ and $0.79 \times 10^5$ $cm^{-1}$. The absorption edge of the doped systems was about 1.5 eV, which corresponded to the calculated bandgap value. Fig. 3(c) shows the reflectance of the three systems, and the enhancement was most obvious in the visible region. At 3.26 eV, the reflectances of the three systems were 28%, 39% and 35%. In the ultraviolet region (3.26–15 eV), the reflectances of the three systems could reach the highest reflectivity of more than 94% at about 13.6 eV. According to the law of conservation of energy, the absorptance and reflectance increased, and the transmittance decreased, which avoided the loss of energy in the form of heat energy through the material, and improved the utilization of energy. Fig. 3(d) shows the loss functions of the three systems, their values in the three systems in the visible region were extremely small (less than 0.1).
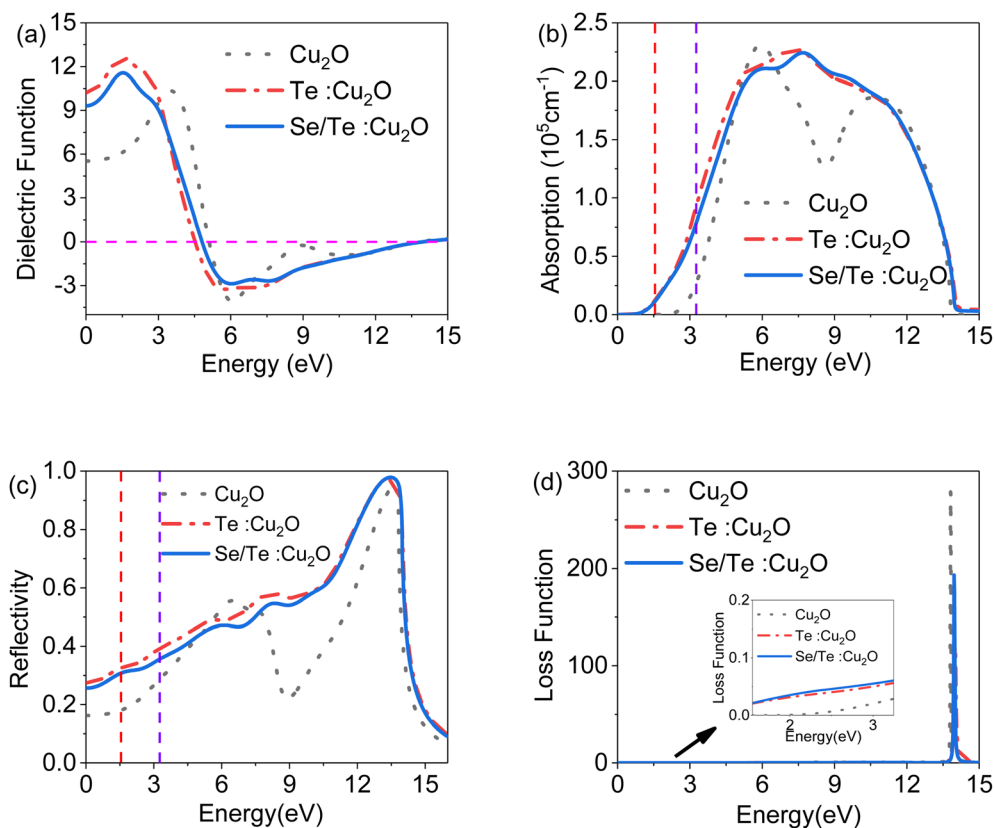


**Fig. 3** The optical properties of pure $Cu_2O$, $Te : Cu_2O$, and $Se/Te : Cu_2O$, (a) the real part of the dielectric function, (b) the absorption spectrum, (c) the reflectance, and (d) the loss function.

# 3 Experimental research

## 3.1 Experiment methods

The theoretical results showed that when the ratios of Te- and Se/Te-doped $Cu_2O$ was 12.5%, the bandgap can reach the infrared region. However, the bandgap of HTL was smaller than that of the PAL (MAPbI$_3$ band gap value of 1.55 eV), which could not take the role of the conduction band to block electrons. Therefore, when preparing samples, the doping ratio was reduced to make the bandgap slightly larger than that of the PAL, and the doping ratio is shown in Table 4. In this experiment, the powders were prepared by solid-phase sintering synthesis,[20,21] and the thin films were prepared by a spin-coating method. The naming of the experimental samples is consistent with that in the theoretical research.

## 3.2 Experimental results and discussion

**3.2.1 XRD, XPS and EDS analyses.** For the XRD characterization, the powders were prepared by experimental details 6.3, and the thin films were prepared by experimental details 6.5, and the results are shown in Fig. 4. The peak position of the $Cu_2O$ powder before and after doping had barely shifted, and its characteristic peak was very sharp, with good crystallinity. The peak of $Cu_2Te$ appeared after that of Te-doped $Cu_2O$. The $Cu_2Te$ belongs to the hexagonal crystal system, the space point group of $P6/mmm$, and the lattice constants were $a = b = 4.18$ Å, $c = 7.237$ Å. Compared with pure $Cu_2O$, the Se/Te-doped $Cu_2O$ showed almost no change in the XRD peaks. Due to the competition between the same group elements, it was difficult to incorporate it into $Cu_2O$.[15] Fig. 4(b) shows the XRD of the thin film, compared with the powder, and the phase of FTO removed by the two doped systems showed almost no change.

For the XPS, the corrected standard C 1s peak position (284.8 eV) is shown in Fig. 5. The peaks of four elements Cu, O, Se, and Te were found, and are identified on the full spectrum shown in Fig. 5(a). Compared with the Te : $Cu_2O$ powder, the peak intensities of Cu 2p and Te 3d of the Se/Te : $Cu_2O$ powder were significantly weakened. Semi-quantitative composition analysis proved that the proportion of Cu and Te was indeed reduced, which was also confirmed by the subsequent EDS analysis. The two splitting peaks of Cu 2p are Cu 2p$_{1/2}$ and Cu 2p$_{3/2}$, and their binding energy positions were about 952.52 eV and 932.76 eV, respectively, which were $Cu^{1+}$. There was only one obvious peak for O 1s, and its binding energy position was about 532.18 eV, which was $O^{2-}$. The two splitting peaks of Te 3d were Te 3d$_{3/2}$ and Te 3d$_{5/2}$, and their binding energy positions were about 583.15 eV and 572.78 eV, respectively, which were $Te^{+4}$. The two peaks near 586.54 eV and 576.04 eV were peaks formed by Te–O bonds, which proved that part of Te occupied the Cu vacancies. There was only one obvious peak for Se 3d, and its binding energy position was about 54.56 eV, which was $Se^{4+}$. The peak positions of the four elements, Cu, O, Se, and Te were basically consistent with those previously reported in the literature.[10,22–24]

Fig. 6 shows the EDS spectra of the Te : $Cu_2O$ and Se/Te : $Cu_2O$ thin films. It can be seen that the proportion of Te in Te : $Cu_2O$ was roughly the same as that in the experimental scheme, and basically it has been doped into $Cu_2O$. The proportion of Se and Te in Se/Te : $Cu_2O$ was very small, about 1%, which was very different from the that found in the experimental scheme. As in the previous analysis, due to the same group elements competing and the large atomic radius difference, it was difficult to dope them into $Cu_2O$. Nevertheless, the results of the XRD, XPS and EDS analyses confirmed that the Se and Te were doped into the $Cu_2O$.

**3.2.2 SEM, AFM, contact angle and Hall analyses.** Fig. 7 shows the SEM images of the Te : $Cu_2O$ and Se/Te : $Cu_2O$ thin films at a scale of 5 μm and 2 μm, respectively. The surface of the thin films prepared by this method show irregularly arranged lumpy particles of different sizes, with many small particles attached to the larger ones, and a very rough surface. The particles of the Te : $Cu_2O$ were more independently distributed than Se/Te : $Cu_2O$, resembling the cubic structure of $Cu_2O$.

Fig. 8 shows the two-dimensional surface and the corresponding three-dimensional AFM images of the Te : $Cu_2O$ and Se/Te : $Cu_2O$ thin films. The surface particles of the two thin films were different in size and irregularly distributed, with

**Table 4** Atomic ratios of the doped systems

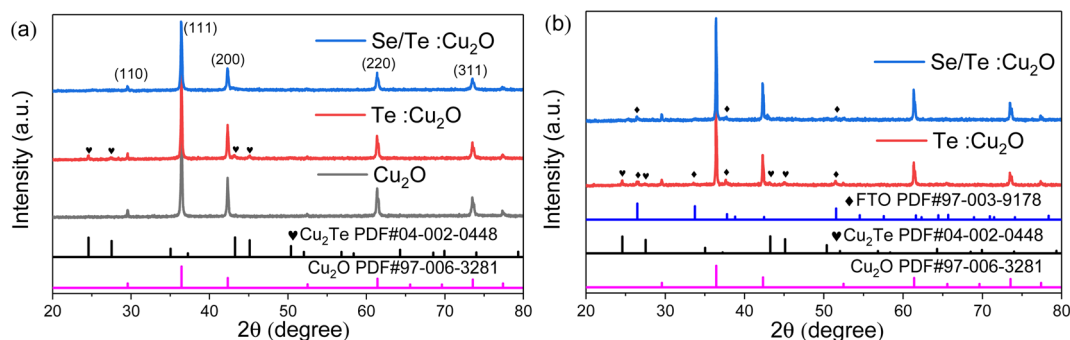|  | $Cu_2O$ | Te | Se | Doping ratio |
|---|---|---|---|---|
| Te : $Cu_2O$ | 2.5 mmol | 0.2 mmol | — | 7.4% |
| Se/Te : $Cu_2O$ | 2.5 mmol | 0.2 mmol | 0.1 mmol | 10.71% |



**Fig. 4** The XRD of (a) pure $Cu_2O$, Te : $Cu_2O$, and Se/Te : $Cu_2O$ powders, and (b) Te : $Cu_2O$ and Se/Te : $Cu_2O$ thin films.
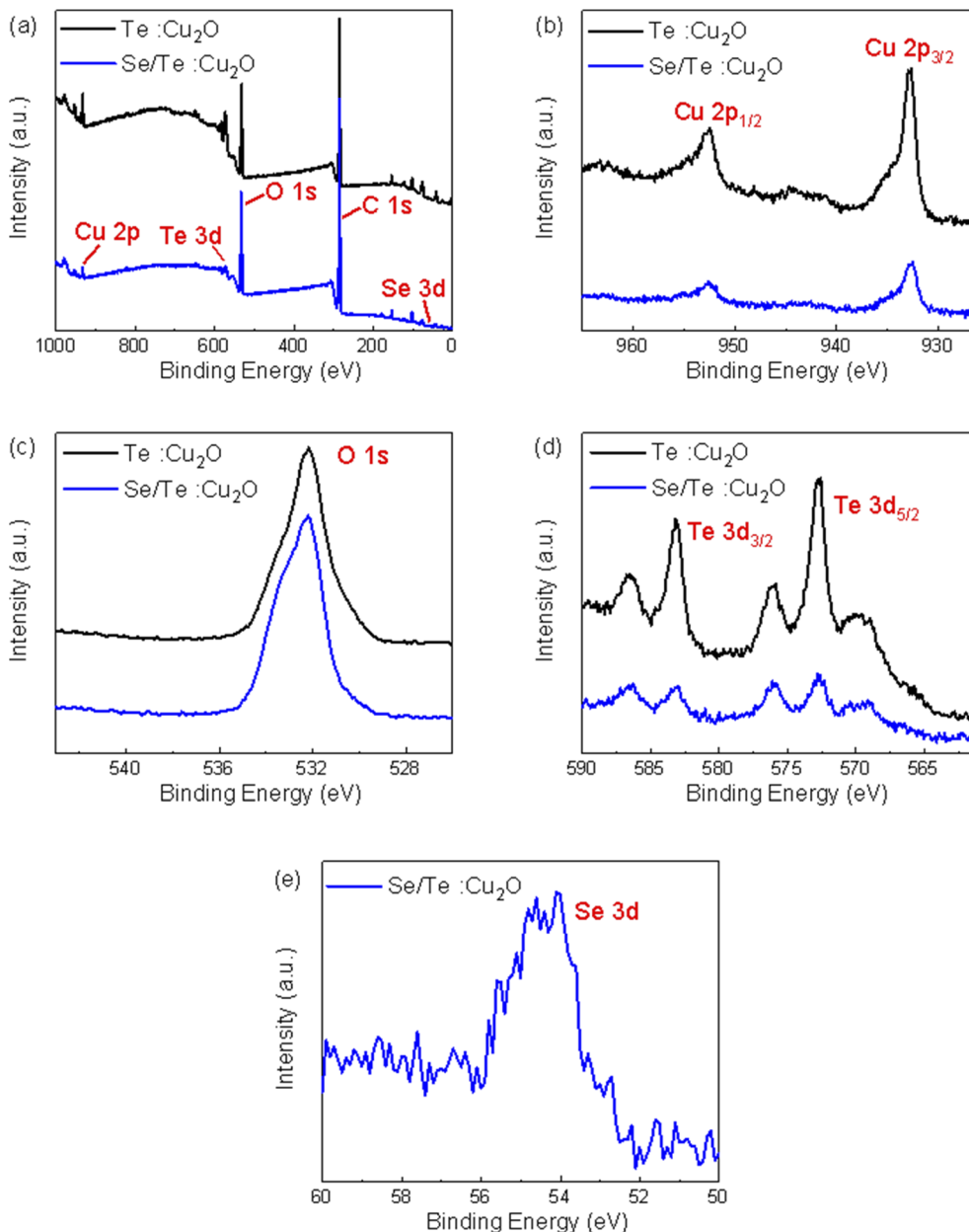
Fig. 5 The XPS spectra of Te : Cu$_2$O and Se/Te : Cu$_2$O powders: (a) full spectra, (b) Cu 2p, (c) O 1s, (d) Te 3d, and (e) Se 3d.

agglomerated large particles, which were caused by solidification during sintering and cooling. The root mean square ($R_{ms}$) of roughness of the Te : Cu$_2$O and Se/Te : Cu$_2$O thin films were 237 nm and 366 nm, respectively. The thicknesses were 2.3 μm and 5.2 μm, respectively. The two thin films were compounded with the FTO substrate, with varying degrees of voids and poor thin film quality.
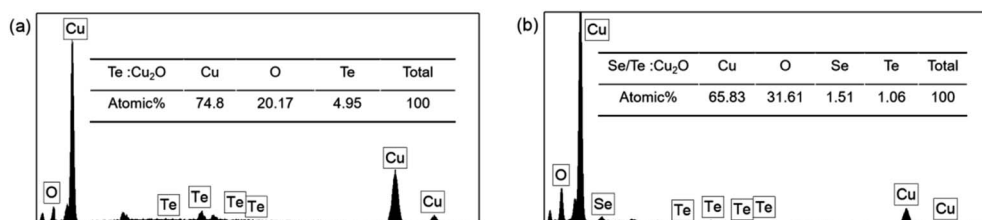


Fig. 6 The EDS spectra of (a) the Te : Cu$_2$O thin film and (b) the Se/Te : Cu$_2$O thin film.
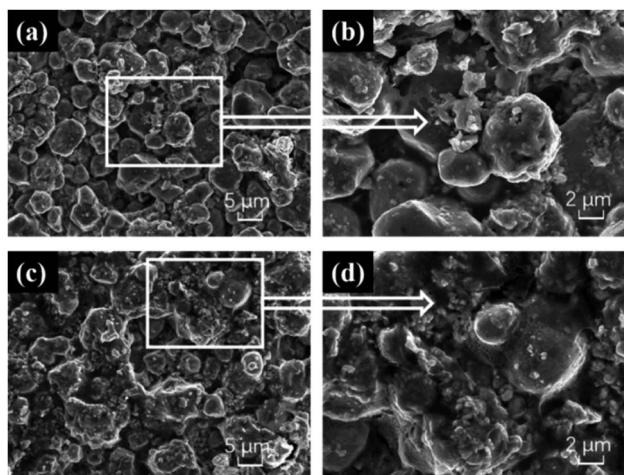
**Fig. 7** The SEM of (a, b) Te : $Cu_2O$ thin film and (c, d) Se/Te : $Cu_2O$ thin film.

Fig. 9 shows the results of the contact angle (CA) analysis of the three thin films. The average CAs of the three systems were 104.32°, 115.15° and 84.848° for 3 μL deionized water, whereas the CA of spiro-OMeTAD was only 67.1°.[25] In contrast, both $Cu_2O$ and $Cu_2O$ doped thin films had better hydrophobic properties and better device stability.

Table 5 shows the characterization parameters of the Hall effect for the three thin films at a temperature of 300 K, where the data of pure $Cu_2O$ are from the literature.[26] The resistivity ($R$) was influenced by both carrier mobility and concentration, and at 300 K, the doped systems had a lower resistivity, higher carrier mobility and higher carrier concentration than the pure $Cu_2O$. The high carrier mobility was produced because of a significant reduction in the effective mass, and was consistent with the results of the analysis of the increase of charge amount due to the emergence of free electrons after doping in the theoretical research, which improved the conductivity of the material.
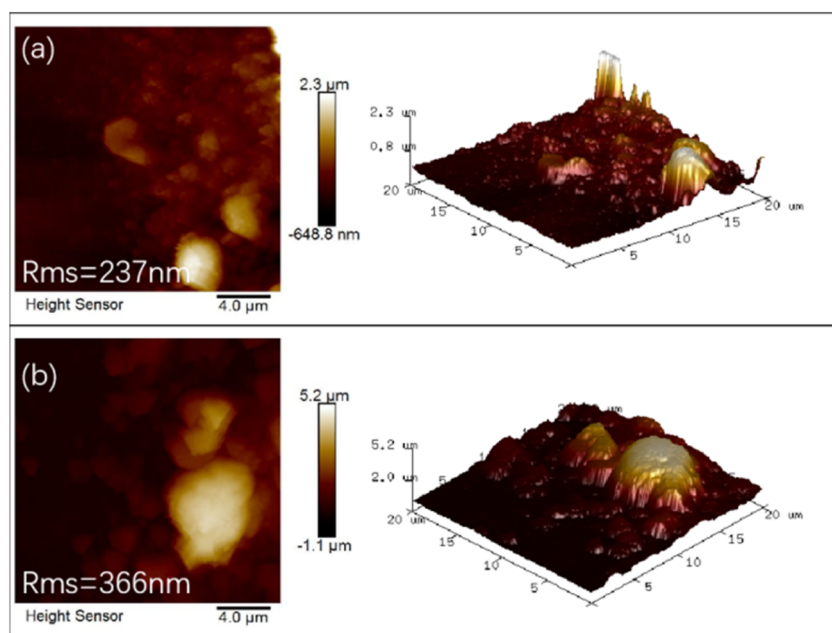


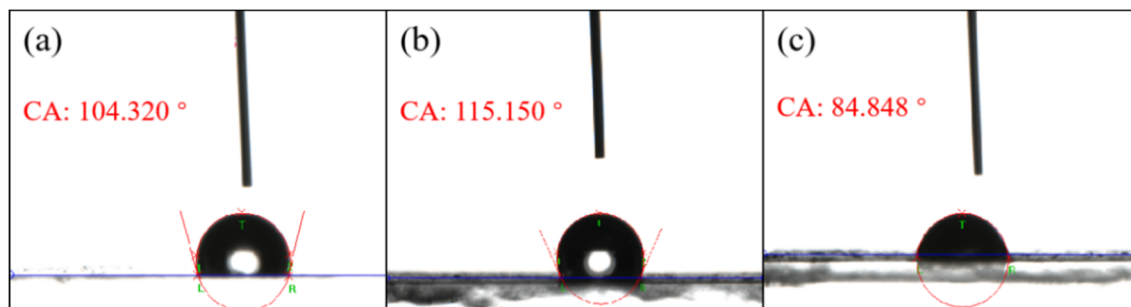**Fig. 8** The AFM images of (a) the Te : $Cu_2O$ thin film and (b) the Se/Te : $Cu_2O$ thin film.



**Fig. 9** Contact angles of (a) the $Cu_2O$ thin film, (b) the Te : $Cu_2O$ thin film, and (c) the Se/Te : $Cu_2O$ thin film.

**Table 5** Characterization parameters of the Hall effect of the Te : $Cu_2O$ and Se/Te : $Cu_2O$ thin films

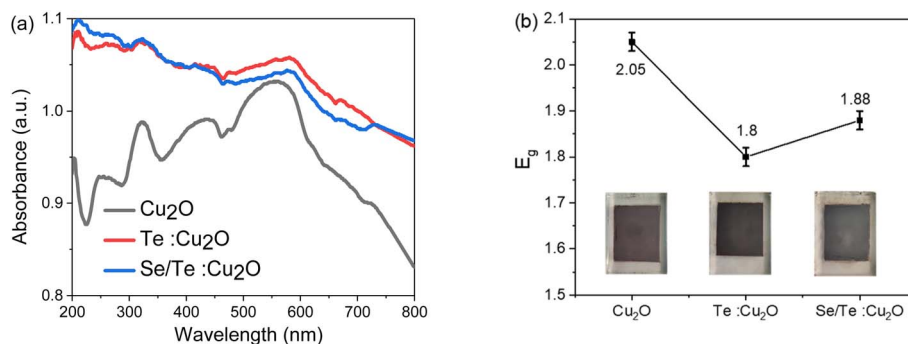| | $R$ (Ω cm) | Mobility ($cm^2 V^{-1} s^{-1}$) | Concentration ($cm^{-3}$) |
|---|---|---|---|
| $Cu_2O$ | $1.35 \times 10^{-3}$ | 60 | $2.0 \times 10^{16}$ |
| Te : $Cu_2O$ | $3.34 \times 10^{-4}$ | 1052 | $1.78 \times 10^{19}$ |
| Se/Te : $Cu_2O$ | $4.13 \times 10^{-4}$ | 1297 | $1.17 \times 10^{19}$ |



**Fig. 10** The UV-vis analysis results of three thin films: (a) absorption spectrum and (b) the corresponding Tauc curves.

**3.2.3 UV-vis and UPS analysis.** Fig. 10 shows the results of the UV-vis analysis of the three thin films. The Te : $Cu_2O$ and Se/Te : $Cu_2O$ had better absorbance than that of pure $Cu_2O$, which was still about 0.95 at 800 nm. The bandgap values of 2.05 eV, 1.8 eV and 1.88 eV for the three films, were obtained from the Tauc plot relationship (Fig. 10(b)), corresponding to the colors of dark-red, black and silver-black, respectively. Considering the doping amount, the experimental bandgap value was in agreement with the expected results.

Fig. 11(a) and (b) show the ultraviolet photoelectron spectroscopy (UPS) of the Te : $Cu_2O$ and Se/Te : $Cu_2O$ thin films, and their Fermi level positions and the relative positions of the valence band edges were fitted. The Fermi level position was the excitation energy of the He–I spectrum (21.2 eV) minus the second ionization potential, and the relative position of the valence band edges was the first ionization potential value.[27,28] In order to determine the energy level position of the doped systems more intuitively and effectively,
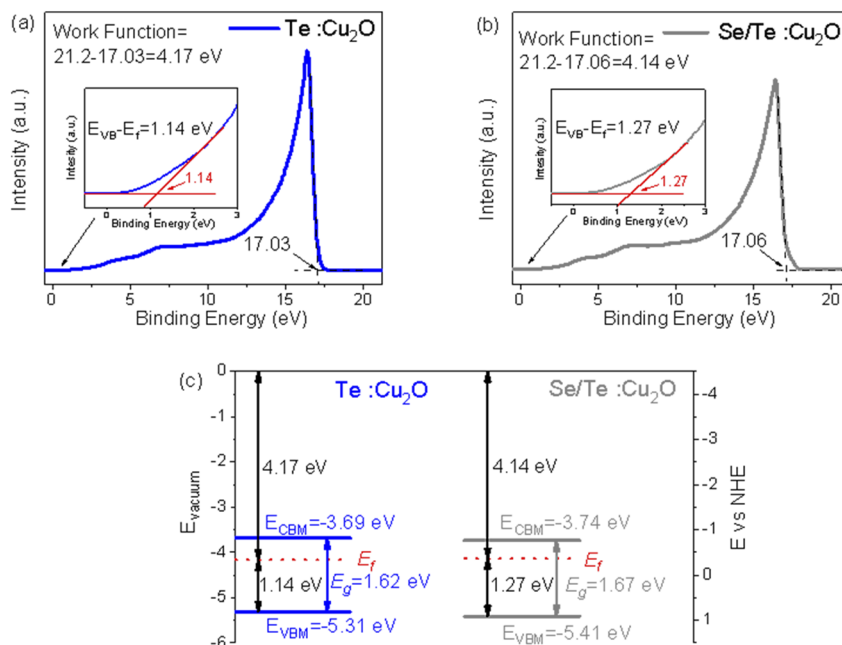


**Fig. 11** (a) UPS results of the Te : $Cu_2O$ thin film, (b) the UPS results of the Se/Te : $Cu_2O$ thin film, and (c) the energy level structure of the Te : $Cu_2O$ and Se/Te : $Cu_2O$ thin films.

**Table 6** Parameters of each layer of the solar cell

| | Spiro-OMeTAD | Cu$_2$O | Te : Cu$_2$O | Se/Te : Cu$_2$O | MAPbI$_3$ | IDL1/2 | TiO$_2$ |
|---|---|---|---|---|---|---|---|
| Thickness (nm) | 400 | 400 | 400 | 400 | 450 | 10 | 50 |
| $E_g$ (eV) | 3.17 | 2.05 | 1.8 | 1.88 | 1.55 | 1.55 | 3.2 |
| $\chi$ (eV) | 2.05 | 3.2 | 3.51 | 3.53 | 3.93 | 3.93 | 4.26 |
| $\varepsilon_r$ | 3.0 | 7.11 | 7.11 | 7.11 | 6.5 | 6.5 | 9 |
| $N_c$ (cm$^{-3}$) | $2.2 \times 10^{18}$ | $2 \times 10^{17}$ | $2 \times 10^{17}$ | $2 \times 10^{17}$ | $2.2 \times 10^{18}$ | $2.2 \times 10^{18}$ | $1 \times 10^{21}$ |
| $N_v$ (cm$^{-3}$) | $1.8 \times 10^{19}$ | $1.1 \times 10^{19}$ | $1.78 \times 10^{19}$ | $1.17 \times 10^{19}$ | $1.8 \times 10^{19}$ | $1.8 \times 10^{19}$ | $2 \times 10^{20}$ |
| $\mu_n$ (cm$^2$ V$^{-1}$ s$^{-1}$) | $2 \times 10^{-4}$ | 80 | 1052 | 1297 | 2 | 2 | 20 |
| $\mu_p$ (cm$^2$ V$^{-1}$ s$^{-1}$) | $2 \times 10^{-4}$ | 80 | 1052 | 1297 | 2 | 2 | 10 |
| $N_D$ (cm$^{-3}$) | 0 | 0 | 0 | 0 | $1 \times 10^{13}$ | $1 \times 10^{13}$ | $5 \times 10^{19}$ |
| $N_A$ (cm$^{-3}$) | $2 \times 10^{19}$ | $3 \times 10^{18}$ | $3 \times 10^{18}$ | $3 \times 10^{18}$ | 0 | 0 | 0 |
| $N_t$ (cm$^{-3}$) | $1 \times 10^{15}$ | $1 \times 10^{15}$ | $1 \times 10^{15}$ | $1 \times 10^{15}$ | $2.5 \times 10^{13}$ | $1 \times 10^{17}$ | $1 \times 10^{15}$ |

Fig. 11(c) was drawn in combination with the bandgap energy level. It can be seen that both Te : Cu$_2$O and Se/Te : Cu$_2$O have good energy level matching with the MAPbI$_3$ ($E_{VBM} = -5.5$ eV, $E_{CBM} = -3.9$ eV) to make efficient transport holes and block electrons.

# 4 Solar cell simulation

## 4.1 Model and parameters

Firstly, a PSC model of FTO/TiO$_2$/IDL1/MAPbI$_3$/IDL2/spiro-OMeTAD/Au was established, and modeled by substituting different HTLs, where IDL1 and IDL2 have interfaced defect layers. Then, the parameters of each layer of the cell were set, as shown in Table 6. The parameters for Cu$_2$O and spiro-OMeTAD were all found from reports in the literature,[29–32] the parameters of Te : Cu$_2$O and Se/Te : Cu$_2$O were mainly from the experimental research, with some using the parameters of Cu$_2$O. The work function of Au was 5.1 eV. Finally, the simulation was

carried out under a temperature of 300 K, standard sunlight AM1.5 G illumination intensity, and the series-parallel resistance was ignored.

## 4.2 Numerical calculation results and discussion

**4.2.1 Results based on different HTLs.** The numerical calculation results are shown in Table 7. The difference in performance between Cu$_2$O-based PSC and spiro-OMeTAD-based PSC was not significant, with the Se/Te : Cu$_2$O-based PSC showing the best performance parameters. The doped Cu$_2$O-based PSCs had an improved $J_{sc}$ when compared to that of Cu$_2$O-based PSC due to the improved carrier mobility enhancement.

**4.2.2 Influence of the HTL thickness on PSCs.** The influence of the HTL thickness of the solar cell performance was explored by changing the thickness of the Se/Te : Cu$_2$O thin film from 50 nm, to 100 nm to 900 nm (at 100 nm intervals), and the final results were calculated, and are shown in Fig. 12. It can be seen that the values of $V_{oc}$, $J_{sc}$ and PCE were on an upward trend with the increase of film thickness, and the increase rate became slow. The fill factor (FF) at 50 nm was 82.5%, after which it started to decrease with the increasing thin film thickness and changed little after 600 nm. Because the Cu$_2$O thin film is a thickness-insensitive material,[33] the low proportion of Se/Te doping may have a minor effect on the film formation, so the Se/Te : Cu$_2$O thin films at different thicknesses had a minor effect on the performance parameters of the PSCs.

**Table 7** Performance parameters of PSCs based on different HTLs

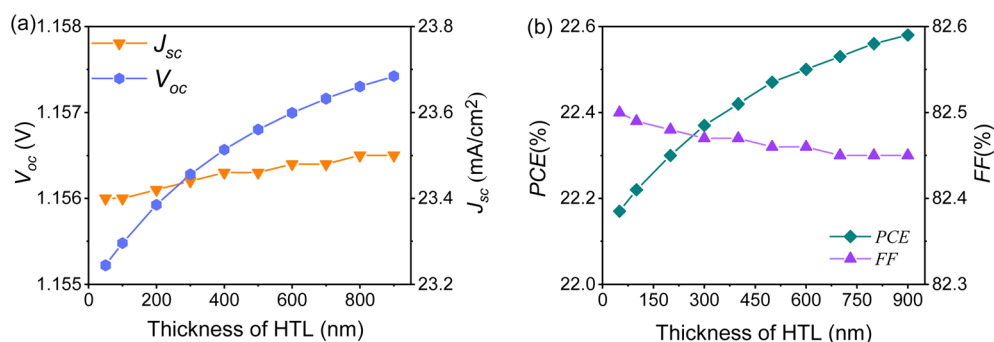| | $V_{oc}$ (V) | $J_{sc}$ (mA cm$^{-2}$) | FF (%) | PCE (%) |
|---|---|---|---|---|
| Spiro-OMeTAD | 1.06 | 23.20 | 74.96 | 18.47 |
| Cu$_2$O | 1.06 | 23.36 | 74.46 | 18.43 |
| Te : Cu$_2$O | 1.08 | 23.60 | 77.69 | 19.96 |
| Se/Te : Cu$_2$O | 1.16 | 23.51 | 82.47 | 22.42 |



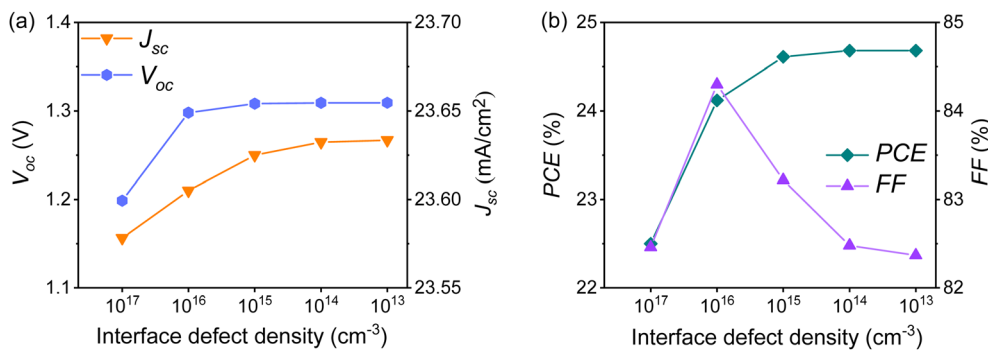**Fig. 12** Performance parameters of PSCs based on HTLs with different thicknesses.

**Fig. 13** Performance parameters of the PSCs based on different IDL densities.

**4.2.3 Influence of the IDL density on PSCs.** The interfacial defects between HTL and PAL, and between ETL and PAL, were unavoidable. Reducing the interface defect density was also used to improve the solar cell performance parameters. In the Se/Te : $Cu_2O$-based PSC, with a thickness of 600 nm, its IDL density was changed to explore the effect on the performance of solar cells. Setting the density in the range of $10^{13}$ $cm^{-3}$ to $10^{17}$ $cm^{-3}$, the final calculated result is shown in Fig. 13. It can be seen when the IDL density was lower than $10^{14}$ $cm^{-3}$, the solar cell's performance reached an optimal stable state, where $V_{oc}$ is 1.26 V, $J_{sc}$ is 23.65 mA $cm^{-2}$, FF is 82.48%, and the PCE is up to 24.68%.

# 5 Conclusions

(1) The theoretical construction of the Te : $Cu_2O$ and Se/Te : $Cu_2O$ models with a 12.5% doping ratio showed a lattice distortion after geometrical optimization, and the bandgaps were 1.489 eV and 1.545 eV, respectively, and the conductivity, absorption coefficient and reflectivity were all improved.

(2) The Te : $Cu_2O$ and Se/Te : $Cu_2O$ with doping ratios of 7.4% and 10.71%, respectively, were prepared experimentally. The doping of Se and Te into $Cu_2O$ was confirmed by the results of XRD, XPS and EDS analysis, and all three thin films had good stability as determined by contact angle analysis, and the improved conductivity of both thin films as determined by the Hall analysis, and both thin films had a good energy level match when comparing with the $MAPbI_3$ properties obtained using UV-vis and UPS analyses. The electrical and optical properties of the Se/Te : $Cu_2O$ thin film were relatively better than the others, which was beneficial for their use as HTL.

(3) Solar cells with four different HTLs were simulated, and the Se/Te : $Cu_2O$-based PSC showed the best performance. After optimization, with the thickness of Se/Te : $Cu_2O$ at 600 nm, and the IDL density at $10^{14}$ $cm^{-3}$, the PCE of the PSCs could reach 24.68%. Compared with the PCE of $Cu_2O$-based PSC, it has increased by 34%.

# 6 Theoretical and experimental details

## 6.1 First-principles calculation

Calculations were made using the CASTEP module in the BIO-VIA Materials Studio software. The exchange-correlation energy was determined by the GGA-PBEsol method. The valence electrons of the atoms were described by the ultrasoft pseudopotential, in which the proportions were set as Cu $3d^{10}4s^1$, O $2s^22p^4$, Se $4s^24p^4$, and Te $5s^25p^4$. The electron wave function was expanded in the plane-wave basis set with a cutoff energy of 440 eV, and a Monkhorst–Pack grid with parameters of a $6 \times 3 \times 3$ $k$-point was used for irreducible Brillouin zone sampling. All the atoms were optimized geometrically by using the Broyden-Fletcher-Goldfarb-Shanno (BFGS) method.

## 6.2 Effective mass calculation

The effective mass of the electrons and holes in the unit of free-electron mass ($m_0$) was estimated by fitting the energy-momentum dependence of the states at the CBM and VBM in the Brillouin zone. Electron effective mass was calculated at the CBM, and hole effective mass at the VBM near the G point in G-F direction, and in the [111] direction.

## 6.3 Powder preparation

$Cu_2O$, Te and Se powders of 99.99% purity were weighed, respectively. The powders were placed into a high-temperature tube furnace with a nitrogen atmosphere for sintering. The melting points of Se and Te were 217 °C and 452 °C, respectively, so they were sintered at 600 °C for 30 min.

## 6.4 Ink preparation

The $Cu_2O$ powder (225 mg), Te : $Cu_2O$ powder (230 mg), and Se/Te : $Cu_2O$ powder (270 mg) were weighed into centrifuge tubes, and 50 μL of deionized water was added to each one. Each solution was mixed ultrasonically for 40 min, and then 30 μL of ethanolamine was added followed by ultrasonic mixing for a further 40 min.

## 6.5 Thin film preparation

The FTOs were placed into a beaker and mixed ultrasonically for 10 min with acetone, absolute ethanol and deionized water, then dried with nitrogen, and then irradiated with UV light for 3 min, for the conversion to a thin film substrate. Then, 10 μL of ink was drop-coated onto the FTO conductive glass surface. The three thin films were prepared by spin-coating at 1200 rpm, 1800 rpm and 1500 rpm for 15 s. The film was placed on a graphite heating plate, heated at 80 °C for 15 min and baked

until semi-dried. The film was trimmed into a 10 × 8 mm shape, and then placed on a graphite heating plate, and heated at 130 °C for 15 min and then baked. Lastly, the thin film was put into a high-temperature tube furnace with a nitrogen atmosphere and annealed at 200 °C for 60 min.

## Author contributions

L. Luo conceived the project, planned and carried out the simulations, performed the experiments and data analysis, and wrote the manuscript. B. Zhou conceived the project, planned and carried out the simulations, and wrote the manuscript. Y. Hu conceived the project. Q. Zhao planned and carried out the simulations. X. Yang planned and carried out the simulations. Z. Liu performed the experiments and data analysis. C. Wang performed the experiments and data analysis. Z. Duan performed the experiments and data analysis. Z. Xie performed the experiments and data analysis. All the authors edited and approved the manuscript.

## Conflicts of interest

The authors declare that they have no known financial interests or personal relationships that could appear to influence the work in this paper.

## Acknowledgements

## References

1 Y. Jiang, H. Yuan and H. Chen, *Phys. Chem. Chem. Phys.*, 2015, **17**, 630–637.

2 R. Zhang, L. Ling, Z. Li and B. Wang, *Appl. Catal., A*, 2011, **400**, 142–147.

3 M. Su, Z. Liang, C. Zhao, P. Liu, S. Yue and W. Xie, *Mater. Lett.*, 2016, **170**, 80–84.

4 G. A. Casas, M. A. Cappelletti, A. P. Cédola, B. M. Soucase and E. L. Peltzer y Blancá, *Superlattices Microstruct.*, 2017, **107**, 136–143.

5 A. M. Elseman, M. S. Selim, L. Luo, C. Y. Xu, G. Wang, Y. Jiang, B. Liu, L. P. Liao, Z. Hao and Q. L. Song, *ChemSusChem*, 2019, **12**, 3808–3816.

6 M. A. Islam, Y. A. Wahab, M. U. Khandaker, A. Alsubaie, A. S. A. Almalki, D. A. Bradley and N. Amin, *Crystals*, 2021, **11**, 389.

7 H. Rao, S. Ye, W. Sun, W. Yan, Y. Li, H. Peng, Z. Liu, Z. Bian, Y. Li and C. Huang, *Nano Energy*, 2016, **27**, 51–57.

8 C.-C. Tseng, L.-C. Chen, L.-B. Chang, G.-M. Wu, W.-S. Feng, M.-J. Jeng, D.-W. Chen and K.-L. Lee, *J. Sol. Energy*, 2020, **204**, 270–279.

9 C. Liu, X. Zhou, S. Chen, X. Zhao, S. Dai and B. Xu, *Adv. Sci.*, 2019, **6**, 1801169.

10 Z.-H. Lin, P. Roy, Z.-Y. Shih, C.-M. Ou and H.-T. Chang, *ChemPlusChem*, 2013, **78**, 302–309.

11 H. Güney and Ç. Duman, *AIP Conf. Proc.*, 2016, **1726**, 020122.

12 Y.-L. Liu, C.-L. Yang, M.-S. Wang, X.-G. Ma and Y.-G. Yi, *Mater. Res. Bull.*, 2018, **107**, 125–131.

13 B. Zhou, L. Luo, Y. Zhang, Y. Hu, Z. Xie, Z. Duan and X. Yang, *Mater. Res. Express.*, 2022, **9**, 035902.

14 X. Ling, Z. Jin, Q. Jiang, X. Wang, B. Wei, Z. Wang, Y. Xu, T. Cao, J. W. Engle, W. Cai, C. Su and Q. He, *Natl. Sci. Rev.*, 2021, **8**, nwaa156.

15 M. M. Obeid, Y. Mogulkoc, S. J. Edrees, Y. O. Ciftci, M. M. Shukur and M. M. H. Al-Marzooqee, *Mater. Res. Bull.*, 2018, **108**, 255–265.

16 C. Zuo and L. Ding, *Small*, 2015, **11**, 5528–5532.

17 X. Zhang, X. Cui, Y. Sun, K. Qi, Z. Jin, S. Wei, W. Li, L. Zhang and W. Zheng, *ACS Appl. Mater. Interfaces*, 2018, **10**, 745–752.

18 X.-G. Yan, L. Xu, W.-Q. Huang, G.-F. Huang, Z.-M. Yang, S. Q. Zhan and J.-P. Long, *Mater. Sci. Semicond. Process.*, 2014, **23**, 34–41.

19 D. Sharma, S. Upadhyay, V. R. Satsangi, R. Shrivastav, U. V. Waghmare and S. Dass, *Appl. Catal.*, 2016, **18**, 75–85.

20 J. Dong, K. Yang, B. Xu, L. Zhang, Q. Zhang and Y. Tian, *J. Alloys Compd.*, 2015, **647**, 295–302.

21 X. Ye, G. Chen, B. Duan and P. Zhai, *J. Electron. Mater.*, 2014, **44**, 1674–1678.

22 M. Behera, R. Panda and R. Naik, *Indian J. Phys.*, 2017, **91**, 555–562.

23 A. Saha, S. Payra, B. Selvaratnam, S. Bhattacharya, S. Pal, R. T. Koodali and S. Banerjee, *ACS Sustainable Chem. Eng.*, 2018, **6**, 11345–11352.

24 D. Rajska, A. Brzózka, M. Marciszko-Wiąckowska, M. M. Marzec, D. Chlebda, K. E. Hnida-Gut and G. D. Sulka, *Appl. Surf. Sci.*, 2021, **537**, 147715.

25 V. M. Arivunithi, H.-Y. Park, S. S. Reddy, Y. Do, H. Park, E.-S. Shin, Y.-Y. Noh, M. Song and S.-H. Jin, *Macromol. Res.*, 2021, **29**, 149–156.

26 S. Ishizuka, S. Kato, Y. Okamoto, T. Sakurai, K. Akimoto, N. Fujiwara and H. Kobayashi, *Appl. Surf. Sci.*, 2003, **216**, 94–97.

27 Y. S. Kwon, J. Lim, H. J. Yun, Y. H. Kim and T. Park, *Energy Environ. Sci.*, 2014, **7**, 1454–1460.

28 Y. Yao, B.-P. Zhang, J. Pei, Y.-C. Liu and J.-F. Li, *J. Mater. Chem. C*, 2017, **5**, 7845–7852.

29 K. R. Adhikari, S. Gurung, B. K. Bhattarai and B. M. Soucase, *Phys. Status Solidi C*, 2016, **13**, 13–17.

30 F. Azri, A. Meftah, N. Sengouga and A. Meftah, *J. Sol. Energy*, 2019, **181**, 372–378.

31 L. Huang, X. Sun, C. Li, R. Xu, J. Xu, Y. Du, Y. Wu, J. Ni, H. Cai, J. Li, Z. Hu and J. Zhang, *Sol. Energy Mater. Sol. Cells*, 2016, **157**, 1038–1047.

32 L. Lin, P. Li, L. Jiang, Z. Kang, Q. Yan, H. Xiong, S. Lien, P. Zhang and Y. Qiu, *J. Sol. Energy*, 2021, **215**, 328–334.

33 S. Maryam, N. Mufti, A. Fuad, Y. A. S. Laksono, A. Taufiq and Sunaryono, *IOP Conf. Ser.: Earth Environ. Sci.*, 2019, **276**, 012035.